Time-of-flight secondary ion mass spectrometry in the helium ion microscope

Klingner, N.; Heller, R.; Hlawacek, G.; Facsko, S.; von Borany, J.;

Originally published:

December 2018

Ultramicroscopy 198(2019), 10-17

DOI: https://doi.org/10.1016/j.ultramic.2018.12.014

Time-of-flight secondary ion mass spectrometry in the helium ion microscope

N. Klingner[a,*], R. Heller[a], G. Hlawacek[a], S. Facsko[a], J. von Borany[a]

[a]*Helmholtz-Zentrum Dresden-Rossendorf e.V., Institute of Ion Beam Physics and Materials Research, Bautzner Landstr. 400, 01328 Dresden, Germany*

Abstract

A helium ion microscope, known for high resolution imaging and modification with helium or neon ions, has been equipped with a time-of-flight spectrometer for compositional analysis. Here we report on its design, implementation and show first results of this powerful add-on. Our design considerations were based on the results of detailed ion collision cascade simulations that focus on the physically achievable resolution for various detection limits. Different secondary ion extraction geometries and spectrometer types are considered and compared with respect to the demands and limitations of the microscope. As a result the development and evaluation of a secondary ion extraction optics and time-of-flight spectrometer that allows the parallel measurement of all secondary ion masses is reported. First experimental results demonstrate an excellent mass resolution as well as high-resolution secondary ion imaging capabilities with sub-8 nm lateral resolution. The combination of high resolution secondary electron images and mass-separated sputtered ion distributions have a high potential to answer open questions in microbiology, cell biology, earth sciences and materials research.

Keywords: helium ion microscope, time-of-flight, elemental analysis, secondary ion mass spectrometry, high resolution imaging

1. Introduction

Secondary ion mass spectrometry (SIMS) instruments are commonly optimized for mass resolution, high yields of large molecules or fast sample throughput while high lateral resolution was only of secondary importance for most designs using a magnetic sector [1–4] as well as for time-of-flight (TOF) instruments [5–7]. To achieve highest positive ion yields typically cesium ions are used as primary particles, while a maximum number of negatively charged secondary ions is achieved by utilizing oxygen ions. Commercially available SIMS instruments can reach spot sizes below 50 nm [8] using cesium, gold or bismuth ions [9–11]. Bismuth and gallium ion beams from liquid metal ion sources can be focused down to perform SIMS with 20 nm resolution [11–16].

In terms of spatial resolution the existing approaches are limited not by the physical extent of the collision cascade but by the relatively large beam diameter. To achieve the highest possible spatial resolution in SIMS the beam diameter has to be sufficiently smaller than the area that secondary ions are sputtered from. The latter is related to the size of the collision cascade and depends on the primary ion species and energy as well as on the target material.

A helium ion microscope (HIM), equipped with a gas field ion source supplying 30 keV helium or neon ions with an extremely high brightness of up to 10^9 A cm^{-2} sr^{-1}, is capable of surface-sensitive imaging with a lateral resolution of 0.5 nm [17–20]. Ion beam milling can be done with 1.8 nm resolution using neon and with 1.3 nm resolution using helium

*Corresponding author
Email address: n.klingner@hzdr.de (N. Klingner)

ions [21]. It currently provides the smallest beam diameter for both imaging and sputtering and as such would be the ideal candidate for high lateral resolution SIMS imaging. With respect to the implementation of SIMS in the HIM, the secondary ion yield for typical beam parameters [22, 23], possible ion extraction geometries [24] and the expected intermixing of layered structures [25] have been studied in previous work. Recently, TOF spectrometry has been implemented in the HIM to measure the energy of backscattered particles [26–28]. In these studies also the first proof of principle experiments on mass spectrometry of sputtered particles have been demonstrated.

An alternative and more sophisticated SIMS setup inside a HIM including an ion extraction optics and a modified Mattauc-Herzog magnetic sector was recently presented by Wirtz et al. [29–31]. A mass resolution $m/\Delta m$ of up to 300 and a lateral resolution of (10.0 ± 3.6) nm for ^{7}Li (75% to 25%) were demonstrated. However, the current implementation of this device is limited by the finite number of detectors and therefore masses that can be detected simultaneously [31]. The setup presented in this work demonstrates lateral highly resolved material analysis with TOF-SIMS in a HIM, that can detect all masses in parallel. In the literature different definitions of the lateral resolution have been used. Since Wirtz et al. demonstrated the highest lateral resolution so far, we used the same criteria for better comparability (75% to 25%). A comparison of different criteria and peak shapes as well as conversion factors has been published by Saeh [32].

2. Instrument Design

2.1. Theoretical considerations

In commercial SIMS machines the primary ion beam spot size typically exceeds the dimensions of the ions collision cascade. Contrary, in the HIM multiple scattered neon or helium projectiles and recoils will create sputtered particles within an area larger than the sub-nm beam spot. We performed binary collision approximation simulations with TRI3DST [33, 34] and evaluated the spatial origin of sputtered particles. The functions of lateral resolution are shown for example in Fig. 1 for 30 keV helium and neon ions impinging on amorphous silicon. The normalized sputter yield per area is plotted versus the distance between the primary ion impact site and the emission site. The yield drops to 50 % in a radius of 1.2 nm for helium and 1.4 nm for neon. Hence, a diameter of 2.4 nm for helium and 2.9 nm for neon approximate the fundamental achievable lateral resolution for imaging of flat surfaces with SIMS. Other target materials of course show slightly different values. The total ion range decreases for lower primary ion energies and for projectiles with higher atomic number. However, the cross section for nuclear collisions and the probability for multiple scattered particles increases at the same time. Therefore, the size and especially the shape of the intensity profile of sputtered particles depend on multiple parameters. In the surrounding area of a pure occurrence of a material, the sensitivity for low concentration is degraded because of the long tails of the lateral resolution function. A small but not negligible fraction of the primary ion beam can cause sputtering of surface material in a distance of up to several 10 nm. For example the sputtering yield drops to 0.1 % in a distance of 8.7 nm from the primary ion impact for helium and 17.4 nm for neon.

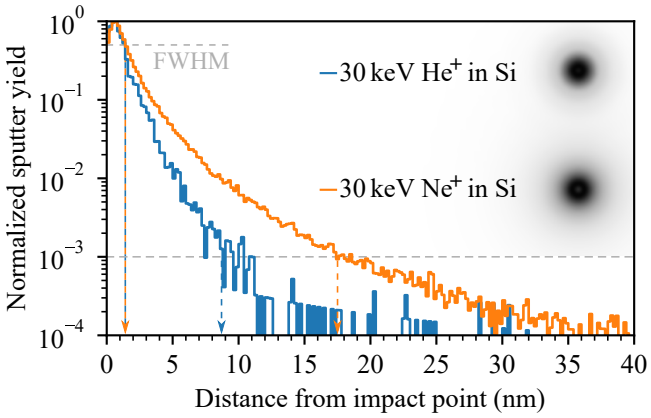

Figure 1: Simulated intensity profiles of sputtered particles in dependence on the distance from the point of impact for 30 keV helium and neon ions in silicon. Emission radii for 50% and 0.1% of the signal intensity are indicated by dashed arrows. The corresponding two-dimensional intensity profiles are shown beside in true dimensions according to the x-axis.

An alternative resolution criteria can be given by the diameter that contains 50 % of all sputtered particles and has been simulated by Wirtz *et al.* [35] to be 3 nm for 30 keV He and 9 nm for 30 keV Ne. Ac-

cording to the TRI3DST [33, 34] simulations used in this work 50 % of all sputtered particles originate from a diameter of 3.6 nm for 30 keV He and 5.9 nm for 30 keV Ne in silicon, respectively. The values are in good agreement for helium but slightly differ for neon projectiles. It has been shown that binary collision approximation simulations deliver similar results as molecular dynamic simulations [36] and experimental data [37]. However, for the prediction of more accurate secondary ion yields especially for non-flat surfaces, three dimensional nanometer sized objects [38] or edge profiles, one has to consider the individual sample geometry, the bulk versus the surface composition, the crystalline structure, as well as ion induced heating effects in more advanced simulations. As SIMS can only deal with secondary ions one has to include the charge exchange processes at the surface in addition to the above listed points. However, the charge exchange process of sputtered particles at the surface is difficult to predict.

For the detection of trace elements in the sample, the achievable lateral resolution is further limited by the finite number of atoms in the interaction volume and the related small number of sputtered ions [22]. Given the small likelihood for a sputtered sample atom to be charged ($\sim 10^{-4}$) one has to remove approximately 250 nm^3 of material to obtain a single secondary ion on average. Furthermore, the depth resolution in the interaction volume will suffer from ion beam damage and mixing [39–41]. Consequently, to maintain low detection limits with shrinking object dimensions, maximization of the extraction and detection efficiencies must be major design considerations. The use of oxygen or cesium primary particles to increase the positive or negative ion yields is unfortunately not an option as the microscope has so far only been designed by the manufacturer for the use of helium and neon gas. However, it has been shown that a gas field ion source can also be operated with other gases like hydrogen [42, 43], nitrogen [43, 44], oxygen [43] or xenon [45]. These ion species could offer many advantages for SIMS and their use will be subject of future investigations. The secondary ion yield can also be enhanced by oxygen gas flooding or cesium coating while using the highly focused Ne or He beam for sputtering [22, 23, 46].

2.2. Selection of mass spectrometer

A major design goal in the present implementation of SIMS in the HIM was the conservation of the outstanding imaging capabilities as well as the modification performance of the instrument. In order to get sufficient signal from the limited amount of sputtered particles the spectrometers extraction, transmission and detection efficiency should be as high as possible. Molecular dynamics simulations and experiments have shown that light atomic projectiles with several keV energy will cause a high molecular fragmentation and mainly produce atomic or short-chain secondary particles [9, 10, 47, 48]. As a consequence the desired mass range doesn't have to exceed 250 u, that would be necessary only for the identification of molecular fragments but not for the detection of single ions or very small molecular fragments.

For the purpose of mass separation ion traps could be utilized, but they can measure only one mass at a time, they often have a high duty cycle and require a precise ion injection. A magnetic sector mass analyzer has less demanding injection conditions and would allow a continuous operation. However, it has to be mounted at the outside of the measurement chamber or the magnetic field has to be shielded from the primary ion beam and the sample region. The spatially mass-separated secondary ions have to be successively detected with either multiple detectors or with a laterally resolving detector. Single ion detectors like micro-channel plates are currently not available to cover larger areas and therefore are limited to a certain mass range [31].

Time-of-flight has the major advantage that the full kinetic energy or mass range can be measured in parallel and no particles are lost as in a serial measurement procedure. Different approaches have been developed in the past to measure the time interval between start and end of the flight path. The time measurement is most commonly stopped by the impact of the particle in a detector at the end of the flight path. For the start signal various solutions are available. The time measurement for instance can be triggered by secondary electrons created during the primary ion impact on the sample surface [49]. To assign the detected particle to the primary ion that created it, the beam current has to be reduced

to less than one primary ion during the maximum flight-time interval. In another approach the measurement can be started by secondary electrons that are emitted when secondary particles are transmitted through a thin carbon foil [50]. That allows in comparison to the previous approach to increase the primary current until one secondary ion is extracted per maximum flight-time interval. Unfortunately, the efficiency and energy resolution of this type of spectrometer are rather low for keV particles making this approach not suitable to be applied in the HIM [51].

Alternatively, the time measurement can be triggered by pulsing the primary or extracted ions [9]. In comparison to the latter approach the beam current does not have to be reduced and an ion pulse can contain a large number of particles. The pulsed extraction of secondary ions was not considered for the discussed application due to less sensitivity since the primary ion beam would also cause sample damage when particles are extracted.

Consequently, the pulsing of the primary ion beam as the most gentle approach was recently implemented in the HIM [26, 28] to enable backscattering spectrometry and SIMS as well. Initially, all primary ions can be deflected into a Faraday cup using the existing blanking plates in the HIM. That prevents the ions from leaving the primary column, hitting the sample surface and thus the creation of secondary particles. Lowering of the blanking voltages to ground potential for a short time window allows primary ions to pass the beam blanker until the blanking voltages are applied again. The time difference between triggering the opening of the beam blanker and the moment when primary ions hit the sample surface is almost constant because of the sharp primary energy [18] and constant propagation times of signals in cables and electronics. Photons that can be created by the primary ion impact can be used to calculate this time difference with the accuracy of the distance between sample and stop detector due to known speed of light [26]. If no photons are available, the time difference must be considered in the time to mass calibration. The spectrometer then just requires a flight tube, a detector at the end and electronics to determine the time difference. For mass spectrometry the secondary ions have to be accelerated and extracted from the surface in order to obtain a sufficient efficiency. The primary pulse length is adjustable between 20 ns (for best mass resolution) and 250 ns (for highest effective current). The pulse generation and characterization as well as backscattering spectrometry were studied and described in detail [26] while TOF-SIMS experiments were just performed as proof-of-principle. Here, we present an optimized TOF-SIMS spectrometer to be used with primary ion beam pulsing that has been designed with the above considerations in mind. Compared to the earlier proof-of-principle experiments, it has a higher mass resolution and improved lateral resolution.

2.3. Secondary ion extraction system

For helium or neon projectiles with energies of several keV the sputtering process is dominated by elastic collisions where secondary particles can be emitted into all directions with an energy up to several eV [52]. An extraction system should be able to collect all positive or negative sputtered ions and direct them towards a detector. The sample is negative or positive biased relative to the extraction system to accelerate charged particles of the same charge state to a uniform energy. Possible extraction geometries in the HIM have been discussed in the past [24]. Dowsett *et al.* [24] showed that a straight nozzle and a flat sample position would lead to an electrical field which is not symmetrical to the extraction optical axis and different sputter emission angles would cause unsymmetrical trajectories and secondary ion beam broadening. The total necessary open diameter for a good ion transmission would exceed the optimal working distance between the ion column and the sample surface (approximately 8 mm) while a larger working distance has a negative influence on the focus spot size. Dowsett *et al.* [24] suggested and implemented an electrostatic sector above the sample to reduce these effects.

Tilting of the sample and a straight extraction geometry leads to a homogeneous electrical field between the sample surface and the opening of the extraction nozzle. A large distance between the sample surface and the extraction system would cause a deflection, astigmatism and aberrations of the primary ion beam between the ion column and the sample surface. However, shrinking of the extraction systems outer dimension would allow the nozzle to be

inserted below the primary column and reduce the extraction distance and the primary beam degradation significantly. Therefore, the tilted straight extraction system was selected as the most suitable geometry for the TOF spectrometer. In both designs, the electrostatic sector as well as in the tilted straight extraction geometry, the primary beam has to be post-aligned in the extraction field.

The three major requirements for the extraction optics are: (1) a full angular collection meaning that secondary ions emitted in all direction are collected, (2) a low working distance, and (3) a high transmission. Secondary goals in the design process include a narrow extracted ion beam, high mass resolution of the overall system and mechanical rigidity of the system. Flight time differences caused by different secondary ion energies and varying flight path lengths should be minimized for highest mass resolution. Those demands could not be satisfied with commercially available solutions that would fit into the limited space.

Therefore, a custom solution and extraction optics was designed using the advanced ion beam transport simulation code package IBSimu [53]. The starting conditions for the sputtered ions were chosen according to a typical angular and energetic distribution spectra of sputtered particles [24, 52] and verified with the angle and energy distribution from TRI3DST. The design of an ion optics is associated with a high number of degrees-of-freedom like distances, diameters, lengths, shape as well as applied voltages on all ion optical elements. Although the time scale for simulating ion trajectories can be as low as some milliseconds nowadays, the simulation of the whole parameter space would not be possible in a finite time. Therefore, an advance optimization strategy can help to find a solution that satisfies the high demands. We developed and applied an evolutionary algorithm to evaluate over 2×10^5 different parameter-sets with a total of 10^8 simulated ion trajectories. The simulation result which revealed the best overall SIMS extraction performance based on just one single accelerating einzel lens is shown in Fig. 2.

A decelerating einzel lens would cause a higher flight time broadening because secondary ions would be slowed down closer to their initial sputter energy, corresponding to larger relative velocity difference. The sample, positioned at a still acceptable working distance of less than 12 mm, has to be tilted towards the extraction nozzle and biased to ±500 V. Trajectories follow symmetrical lines around the extraction axis and the majority of the ions are focused to the end of the flight path. A fine grid at the nozzle entrance ensures straight field lines and avoids a divergent lens effect when ions enter the extraction. The simulations reveal high extraction efficiency and low aberrations of the primary beam. Performance tests shown later in this paper confirm these findings.

Additionally, electrostatic steering plates for fine alignment are integrated in the final design. A rendering of the overall setup is shown in Fig. 3. The extraction nozzle is fully retractable and can be aligned mechanically by micrometer calipers on the outside of the microscope. All parts facing the inside of the measurement chamber are at ground potential and should therefore not influence the microscope performance.

3. Results and discussion

3.1. Mass Spectra

In order to evaluate and calibrate the setup, various well characterized samples have been analyzed. From more than twenty (known) mass peaks the time-of-flight to mass calibration was derived. The calibrated mass spectra have been rebinned to an equal bin width. A positive ion mass spectrum of a silver surface is shown as an example in Fig. 4. A primary beam of 25 keV Ne^+ with a current of 10 pA was utilized to obtain a high sputter yield while having a reasonable ion beam spot size. For the used repetition rate of 10 kHz this results in an effective current of approximately 3 fA. As described earlier, longer pulse widths can be applied to reduce the measurement time when mass resolution is less important. Short ion pulses can also cause a broadening of the primary ion beam [27]. For SIMS imaging with highest lateral resolution, a pulse width longer than 100 ns should be applied to minimize this broadening effect.

Besides both silver isotopes, typical organic molecular fragments such as CH_3^+ and $C_4H_9^+$ with several intermediates and traces of sodium and hydrogen show

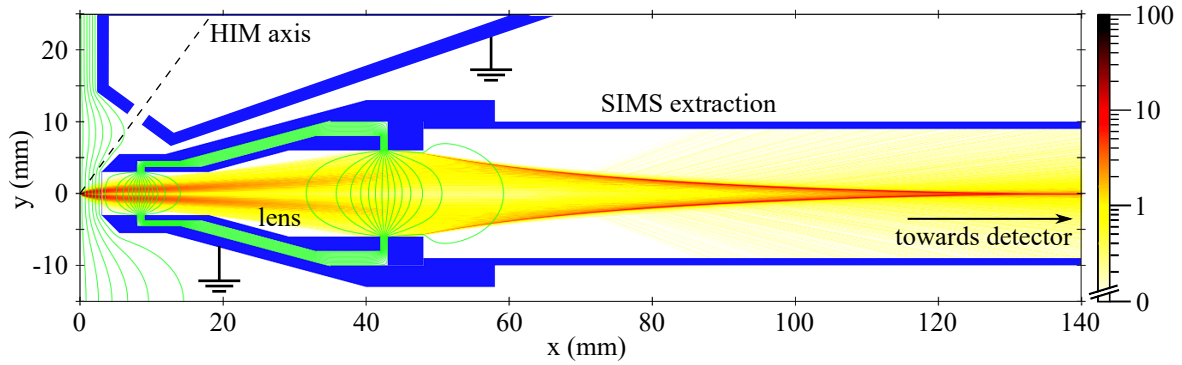

Figure 2: Ion optical simulation of the secondary ion extraction system. Tilted sample is aligned with the y-axis, primary ions incident on the origin of ordinates and create 5000 secondary ions with an initial energy and angular distribution of the sputtered particles. Secondary particle density is calculated and shown on a logarithmic scale.

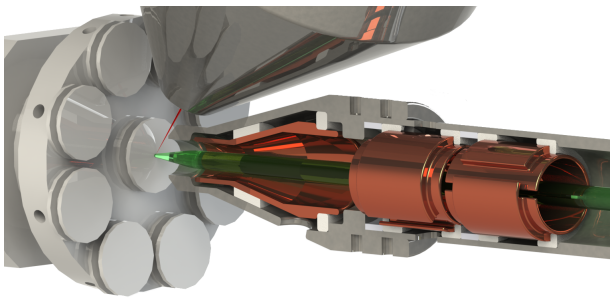

Figure 3: Scheme of primary ion column, sample holder and sectional view of the secondary ion extraction system. Primary ion beam in red, extracted secondary ions in green, electrical isolators white and ion optical elements copper-coloured.

up in the mass spectra. The molecular fragments originate either from surface contamination or from adsorbed residual gas from within the chamber. Although all experiments have been performed at a pressure of $\sim 10^{-7}$ mbar a significant deposition from the gas phase takes place during the acquisition. According to the Hertz-Knudsen-equation, within a typical acquisition time of 10 min more than one monolayer of hydrocarbons attaches the surface from the gas phase. Thus, even *in-situ* plasma cleaning prior to the measurements would be insufficient to completely avoid residual gas mass peaks. Therefore, in future designs a vacuum of at least 10^{-9} mbar would be highly desirable.

Peaks below $m/q = 80$ u show a mean width of (0.26 ± 0.09) u. At these masses, the resolution is sufficient for isotope separation which could be of particular interest in applications like isotope labeling in life science. In all measured spectra the peaks originating from bulk elements are far more broadened than the finite mass resolution of the spectrometer and show an asymmetric peak broadening towards shorter flight times or respectively lower masses. The $^{107}Ag^+$ peak has full width at half maximum Δm of 1.68 u and the $^{109}Ag^+$ has a Δm of 1.56 u.

In order to understand the origin of this broadening we simulated the energy and angular distribution of sputtered silver particles. The initial energy distribution of all sputtered particles before extraction has been simulated with TRI3DST [33, 34] (Fig. 5(a) blue). The relative large amount of sputtered particles with energies above 10 eV can be assigned to nuclear collisions with a relatively high energy transfer either with backscattered primary ions or recoils. These scattering events most probably take place below the first monolayers and would therefore in literature be referred as recoils.

Further, the binary collision approximation code is not able to provide the charge state of sputtered particles. The ionization probability of sputtered particles should in general increase towards higher energies [54–56]. For energies below 5 eV or inverse velocities above 5 µs/cm the secondary ion formation is still subject of current research [57, 58]. We did not include the charge state in our simulations since the theoretical models still deviate from the rare experimental data.

The efficiency (extraction and transmission) of the ion extraction system for sputtered particles has been simulated in ion beam transport calculations using IBSimu [53] (Fig. 5(a) green). Since the extraction system was designed to extract secondary ions with energies up to 10 eV, the loss of efficiency at

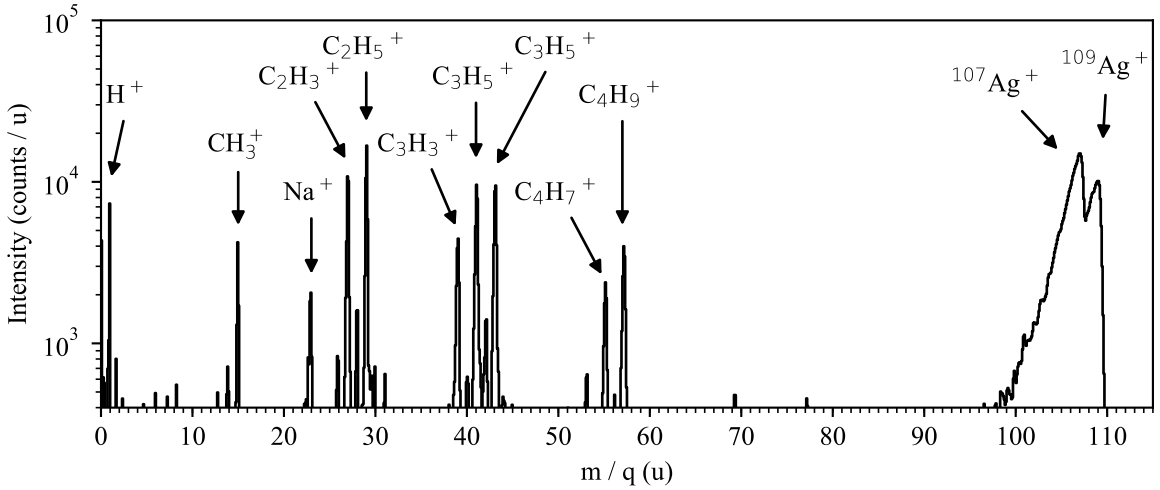

Figure 4: Positive ion mass spectrum of a silver surface (black). Primary beam: 25 keV Ne^+, 30 ns pulse length, 10 kHz repetition rate, 3 fA effective current, 3×10^{12} ions cm^{-2}.

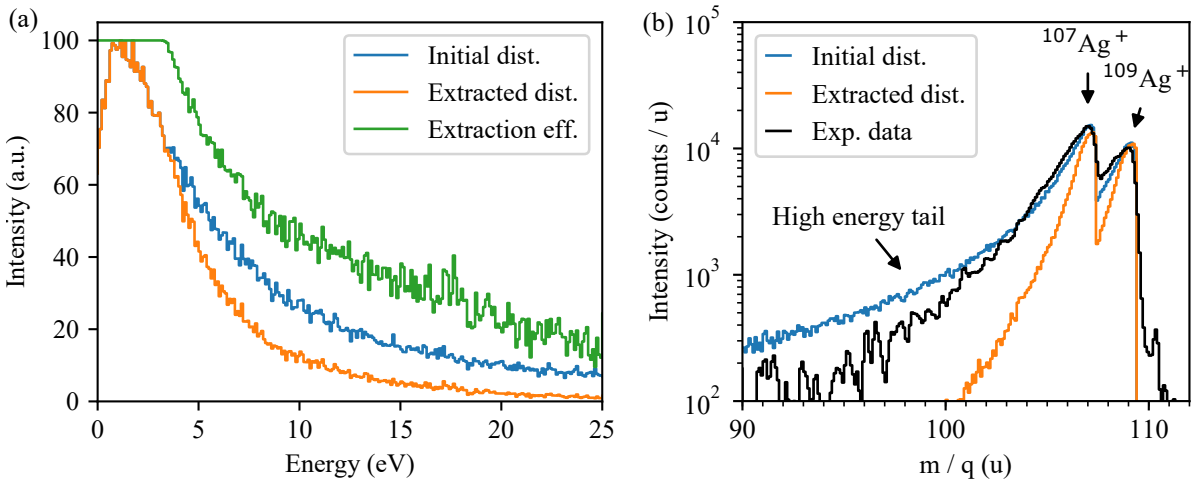

Figure 5: (a) Normalized energy distribution of sputtered Ag particles from TRI3DST summed up over all sputtering angles (blue). Extracted and transmitted particles (orange) according to ion transport simulations using IBSimu [53] and derived efficiency of the SIMS extraction optics (green). (b) Corresponding mass spectra of the initial (blue) and extracted, transmitted silver particle distribution (orange). In comparison the experimental Ag spectrum (black).

higher energies is attributed to insufficient focusing of the einzel lens. The gentle drop of intensities towards higher energies can be explained since a portion of sputtered ions are emitted perpendicular to the surface and straight into the extraction system and therefore do not have to be focused by the ion optics.

The resulting energy distribution of extracted sputtered particles is shown in Fig. 5(a) (orange line). By comparing initial and extracted intensity we get a theoretical total efficiency of (60 ± 1) % assuming the energetic and angular distribution extracted from TRI3DST simulations. The total efficiency for sputtered positive or negative ions can be different from this value. Since the ionization probability decreases at lower energies where the extraction efficiency is high we expect slightly lower total efficiencies for charged particles. However, a quantitative estimation is difficult, since the energy distribution of charged particles depends on many parameters, including varying projectile target combinations and even the sample temperature [59].

The described differences in the energy of sputtered particles as well as different trajectory lengths will lead to a broadening of the flight time. Since in the time to mass calibration a sharp sputtering energy of 3 eV and a fixed flight path was assumed, these de-

viations consequently result in an error of the mass to charge state ratio m/q and therefore contribute to the observed peak broadening. The initial energy distribution from TRI3DST has been converted, rebinned and adjusted to the measured signal intensity for both silver isotopes assuming a natural isotope ratio (see Fig. 5(b) in blue). The same has been applied to the data corresponding to the orange line in Fig. 5(b). The discrepancy between experimental data and simulation results (black and orange line in Fig. 5(b)) according to the above considerations may be attributed to the neglected dependence of the secondary particles charge state on their energy and angle of emission. Another explanation could be misalignment of the extraction optics or ion optical elements which were not considered in the simulation. If a particular charge fraction function of sputtered particles would be known and considered in the above simulations, the simulated and experimental data would be in better agreement. However, the charge fraction as a function of ion energy and emission angle is not available from literature in the energy range applied in this work.

Contrary to the bulk signal, the molecular fragments exclusively originate from the first atomic layers and a high energy transfer scattering event is unlikely. Those particles can be emitted in a rather soft collision in the recoil cascade and therefore have a narrower energy distribution. A high energy collision would also result in higher fragmentation of these molecular fragments.

The mass resolution for bulk components can be increased by using a higher acceleration voltage for the secondary ions to reduce the relative ion energy spread. However, this would require a custom sample holder that can be biased to more than ±500 V. Alternatively, one could use a conventional reflectron TOF design to compensate for the energy spread of sputtered particles. The latter would also result in a higher time or mass resolution due to the extension of the TOF. Therefore, the current setup was designed in a way that a later integration of a reflectron optics is easily possible.

3.2. Imaging SIMS

Besides the analysis of the composition for a certain object of interest, SIMS can be utilized to generate element distribution maps on a very small lateral scale. In this mode, instead of the evaluation of the secondary electron (SE) yield, the yield of sputtered ions is used for contrast generation. Both, the total ion yield as well as the particular yield of a single ion mass can deliver valuable information that are not accessible from SE images. While a total ion yield image reveals good element contrast, mass selected mapping allows the precise determination of the location and the distribution of one particular element.

Examples for both imaging modes are shown in Fig. 6 for two different samples. A copper transmission electron microscopy grid on top of copper scotch tape Fig. 6(a-c) and a NaCl micro and nanocrystal on a silicon substrate Fig. 6(e-i). Table salt was crushed on a silicon substrate to get micrometer and nanometer sized crystals of NaCl. It provides a sample with high yield of positive sodium and negative chlorine ions that is easy to obtain and prepare to reproduce the shown results. Additionally, the integrated mass spectrum (sum of all pixels) of the latter sample is seen in Fig. 6(i). The dwell time (data acquisition time per pixel) was chosen to be a couple of milliseconds to ensure multiple primary ion pulses in each pixel.

Fig. 6(c) represents a demagnification of the area shown in Fig. 6(b). It reveals the area of the previous imaging by a higher intensity, an effect that can be attributed to the removal of surface contaminants, surface roughening, or compositional changes induced by the ion beam.

For the secondary electron images in Fig. 6(d) an ion fluence of $10^{14}\,\mathrm{Ne^+cm^{-2}}$ was applied whereas the SIMS measurement in Fig. 6(e-g, i) was done with $3.8 \times 10^{12}\,\mathrm{Ne^+cm^{-2}}$ and in Fig. 6(h) with $2.1 \times 10^{15}\,\mathrm{Ne^+cm^{-2}}$. The irradiated areas typically suffer from severe sample damage and in this case from sputtering in the exposed area and redeposition close by (indicated by green arrows in Fig. 6(d)). They are visible as black squares with a bright surrounding on the presented NaCl micro-crystal in the post-SIMS secondary electron image (see Fig. 6(d)).

The lateral resolution of the presented setup was studied on multiple edges with different orientations. Therefore a NaCl micro-crystal was partially irradiated, on the area indicated by dotted lines in Fig. 7(a),

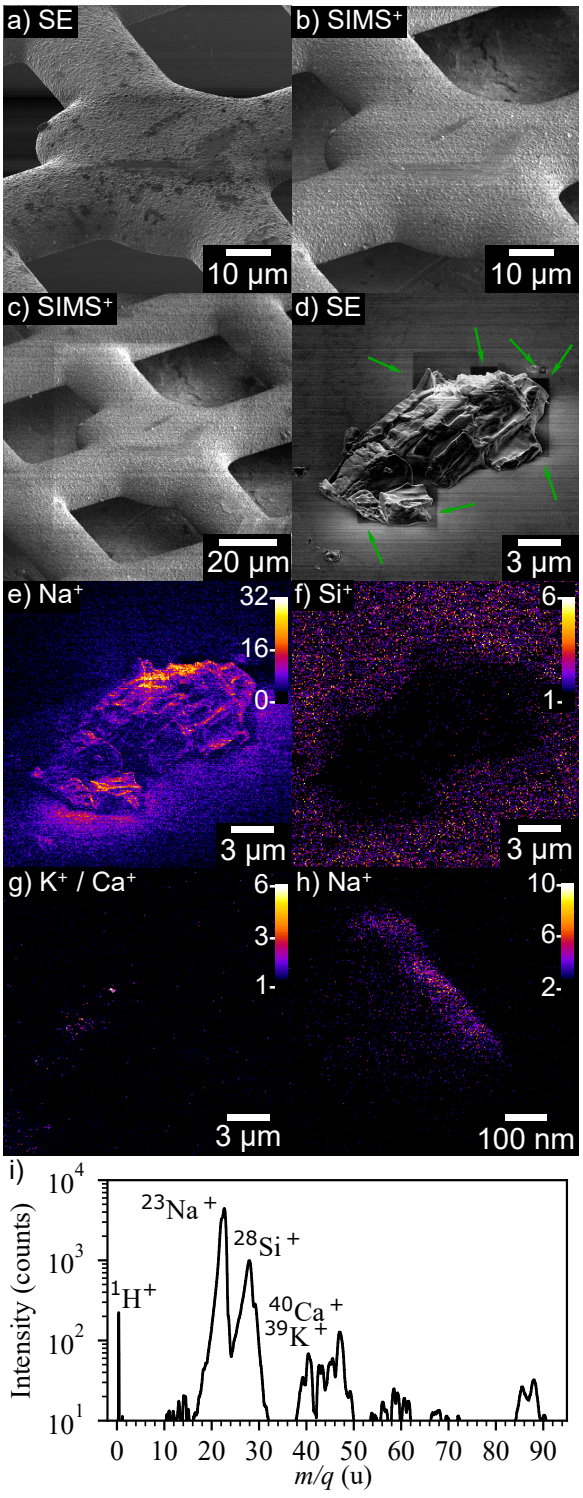

Figure 6: Images of a transmission electron microscope grid as generated by a 25 keV Ne^+ beam (a-c) (1024×1024 pixels). The contrast is generated by secondary electron yield (a) and the positive secondary ion yield (b,c). Secondary electron image, ablation in exposed areas and sputter redeposition close by is indicated by green arrows (d), SIMS element maps (e-g) and integrated SIMS spectrum (i) of a NaCl micro-crystal and Na^+ map of a NaCl nano-crystal (h). The measurements (e-i) were recorded with 25 keV Ne^+, a pixel resolution of 256×256, 150 ns pulses with 18 kHz repetition rate and 2.5 fA effective current. A 20 µm (e-g) / 700 nm (h) field of view, 15 ms (e-g) / 10 ms (h) dwell time per pixel and a total acquisition time of 16 min was used in (e-g) or rather 11 min in (h). The color of maps represents the number of counts per pixel (see color scale).

with the spectrometer inserted and the extraction field applied. The irradiation was performed with a 0.5 pA, unpulsed 25 keV neon ion beam using a fluence of around $10^{18}\,Ne^+cm^{-2}$ at 54° incident angle. During the irradiation and the measurements the sample holder was tilted towards the extraction system, see Fig. 2. All of the following milling and analysis steps have been performed with the inserted ion extraction optics and with enabled extraction bias.

The majority of the measured sputtered ions in positive mode are sodium ions (see Fig. 6(i)). To avoid a low duty cycle and a reduced effective beam current, an unpulsed beam was used for imaging to get a better signal to noise ratio in the same measuring time. The total sputtered ion yield was used to create an image contrast which is influenced for example by the elemental composition and the charge state of secondary particles. The latter is itself influenced by the surface chemistry and the local work function. Furthermore, the collision cascade and the extraction efficiency depend on the surface topography which dominates in the present case the contrast mechanism.

The signal intensity, and therefore the amount of sputtered ions that can be measured in the irradiated areas of the sample is lower compared to the unirradiated area. The sodium chloride crystal was either partially or completely removed in the milled area. The lower total yield of positive secondary ions in the irradiated area can be explained by a reduced extraction efficiency and a reduced emission of secondary ions from the milled trenches [60, 61]. The signal intensity however is higher directly next to the irradiated areas. This is specially seen on those edges that are on the top left of the trenches. The secondary electron yield dependence on the incident angle and on surface topography has been investigated before in scanning electron microscopes [62] and focused ion beam instruments including HIMs [63–65]. Secondary electrons as well as ions are created when the primary ion enters the sample surface, but more importantly for this effect, also when the primary ion or secondary particles leave the sample. Therefore a similar signal enhancement on edges and topographic effects are expected for the secondary ion yield as well. This is in agreement with binary collision approximation (BCA) simulations [33, 34]. The

enhanced secondary ion yield from surface edges was also observed in other SIMS measurements in the HIM [31].

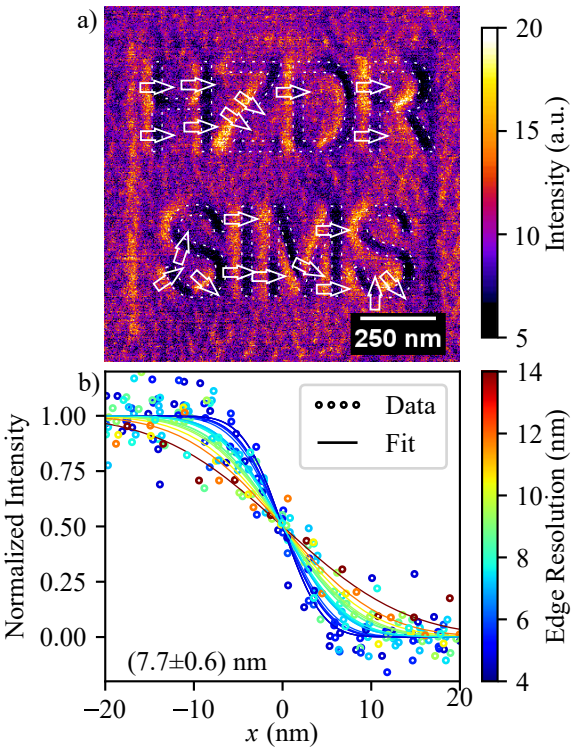

Figure 7: NaCl crystal with ion beam engraved text (marked by dotted lines) as imaged using the total positive secondary ion yield (a). Measurement time of 105 s, 0.5 pA, unpulsed 25 keV neon ion beam, 20 µm aperture, spot control 4 or crossover position at −211 mm, 400×400 pixels and a field of view of 1.2 µm. The number of secondary ions per pixel has been estimated based on the secondary ion yield per primary ion measured in Fig. 6(i). 20 edge profiles have been extracted from the areas indicated by the arrows in the total ion yield image. Each of these edge profiles was averaged over a width of 12 pixels respectively 36 nm, normalized and fitted by an error function (b). For better visualization the edge profiles have been aligned to the fitted center of the error function. Data points as well as fit functions are colored according to their edge resolution (75 % to 25 %). The mean edge resolution evaluates to (7.7 ± 0.6) nm.

Several edge profiles were extracted from the total positive secondary ion image (see Fig. 7(a)), averaged as indicated by the width of the arrow (12 consecutive lines or 36 nm each), normalized and fitted by a simple error function (b). The lateral resolution was defined as the intensity drop from 75 % to 25 % and indicated as color of the particular data points and fit functions. The mean edge resolution obtained from the 20 averaged edge profiles is 7.7 nm with a standard deviation of 0.6 nm.

We thus demonstrated that sputtered particles can be extracted with a lateral resolution close to the fundamental limit of SIMS on flat samples, which has been estimated to be 3 nm (see Fig. 1). It should be emphasized that the lateral resolution alone does not take into account the sensitivity to certain ions. It will therefore not be possible to extract sufficient ions of each sample component from a sputter volume whose diameter is in the order of the lateral resolution. Therefore, highest lateral resolution is achieved exclusively for elements providing a high secondary ion yield.

Additionally, it has to be mentioned that our measurements were not carried out on a flat surface and are therefore not directly comparable with the simulation results. Furthermore, due to the sputtering process the surface topography changes continuously which will certainly influence the shape of edges during the data acquisition. Although we demonstrated highest lateral resolution of 7.7 nm, the ultimate resolution could not be achieved in this work since the low signal intensity and the quickly occurring sample damage hamper the precise focusing of the primary ion beam in the applied extraction field. In future work the influence of the extraction field on the primary ion beam will be studied to speed up the switching between normal secondary electron imaging and material analysis using SIMS.

4. Conclusions

TOF-SIMS was implemented in a HIM with a tilted and biased sample and a straight secondary ion extraction geometry. The implemented setup was simulated with IBSimu, optimized for a high efficiency using an evolutionary algorithm and experimentally studied on various samples. High transmission, a mass resolution of 0.3 u and 8 nm edge resolution have been demonstrated.

Sample damage and detection limits which are a function of the sputtered volume used during the analysis of nano structures are a fundamental limitation of sputtering based analysis methods in particular for the low amount of available sample material. However, with the demonstrated mass resolution and the resulting ability to separate isotopes for light elements in combination with the record lateral reso-

lution give the method a large potential for material analysis in life sciences, material science and other research fields.

Acknowledgement

Financial support from the Bundesministerium für Wirtschaft und Energie (BMWi) (Grant 03ET7016) and the Bundesministeriums für Bildung und Forschung (BMBF) (Grant 03THW12F01) is acknowledged. The authors thank R. Aniol (HZDR) for manufacturing of the mechanical parts.

References

[1] H. Liebl, Ion Microprobe Mass Analyzer, Journal of Applied Physics 38 (13) (1967) 5277–5283. doi:10.1063/1.1709314.

[2] G. D. Schilling, F. J. Andrade, Barnes, R. P. Sperline, M. B. Denton, C. J. Barinaga, D. W. Koppenaal, G. M. Hieftje, Characterization of a Second-Generation Focal-Plane Camera Coupled to an Inductively Coupled Plasma MattauchHerzog Geometry Mass Spectrograph, Analytical Chemistry 78 (13) (2006) 4319–4325. doi:10.1021/ac052026k.

[3] N. T. Kita, J. M. Huberty, R. Kozdon, B. L. Beard, J. W. Valley, High-precision SIMS oxygen, sulfur and iron stable isotope analyses of geological materials: accuracy, surface topography and crystal orientation, Surface and Interface Analysis 43 (1-2) (2011) 427–431. doi:10.1002/sia.3424.

[4] A. K. Schmitt, T. Zack, High-sensitivity U-Pb rutile dating by secondary ion mass spectrometry (SIMS) with an O 2 + primary beam, Chemical Geology 332-333 (2012) 65–73. doi:10.1016/j.chemgeo.2012.09.023.

[5] A. Benninghoven, Developments in secondary ion mass spectroscopy and applications to surface studies, Surface Science 53 (1) (1975) 596–625. doi:10.1016/0039-6028(75)90158-2.

[6] A. Benninghoven, Chemical Analysis of Inorganic and Organic Surfaces and Thin Films by Static Time-of-Flight Secondary Ion Mass Spectrometry (TOF-SIMS), Angewandte Chemie International Edition in English 33 (10) (1994) 1023–1043. doi:10.1002/anie.199410231.

[7] J. C. Vickerman, D. Briggs, ToF-SIMS: Materials Analysis by Mass Spectrometry, SurfaceSpectra, 2013.

[8] P. Hoppe, S. Cohen, A. Meibom, NanoSIMS: Technical Aspects and Applications in Cosmochemistry and Biological Geochemistry, Geostandards and Geoanalytical Research 37 (2) (2013) 111–154. doi:10.1111/j.1751-908X.2013.00239.x.

[9] F. Kollmer, Cluster primary ion bombardment of organic materials, Applied Surface Science 231-232 (2004) 153–158. doi:10.1016/j.apsusc.2004.03.101.

[10] D. Touboul, F. Kollmer, E. Niehuis, A. Brunelle, O. Laprévote, Improvement of biological time-of-flight-secondary ion mass spectrometry imaging with a bismuth cluster ion source, Journal of the American Society for Mass Spectrometry 16 (10) (2005) 1608–1618. doi:10.1016/j.jasms.2005.06.005.

[11] F. Kollmer, W. Paul, M. Krehl, E. Niehuis, Ultra high spatial resolution SIMS with cluster ions - approaching the physical limits, Surface and Interface Analysis 45 (1) (2013) 312–314. doi:10.1002/sia.5093.

[12] R. Levi-Setti, G. Crow, Y. L. Wang, Imaging SIMS at 20 nm Lateral Resolution: Exploratory Research Applications, 1986, pp. 132–138. doi:10.1007/978-3-642-82724-2_31.

[13] J. Orloff, Fundamental limits to imaging resolution for focused ion beams, Journal of Vacuum Science & Technology B: Microelectronics and Nanometer Structures 14 (6) (1996) 3759. doi:10.1116/1.588663.

[14] B. Tomiyasu, I. Fukuju, H. Komatsubara, M. Owari, Y. Nihei, High spatial resolution 3D analysis of materials using gallium focused ion beam secondary ion mass spectrometry (FIB SIMS), Nuclear Instruments and Methods in Physics Research Section B: Beam Interactions with Materials and Atoms 136-138 (1998) 1028–1033. doi:10.1016/S0168-583X(97)00790-8.

[15] T. Sakamoto, M. Koizumi, J. Kawasaki, J. Yamaguchi, Development of a high lateral resolution TOF-SIMS apparatus for single particle analysis, Applied Surface Science 255 (4) (2008) 1617–1620. doi:10.1016/j.apsusc.2008.05.153.

[16] M. Senoner, A. Maaßdorf, H. Rooch, W. Österle, M. Malcher, M. Schmidt, F. Kollmer, D. Paul, V.-D. Hodoroaba, S. Rades, W. E. S. Unger, Lateral resolution of nanoscaled images delivered by surface-analytical instruments: application of the BAM-L200 certified reference material and related ISO standards, Analytical and Bioanalytical Chemistry 407 (11) (2015) 3211–3217. doi:10.1007/s00216-014-8135-7.

[17] B. W. Ward, J. A. Notte, N. P. Economou, Helium ion microscope: A new tool for nanoscale microscopy and metrology, Journal of Vacuum Science & Technology B: Microelectronics and Nanometer Structures 24 (6) (2006) 2871–2874. doi:10.1116/1.2357967.

[18] J. A. Notte, B. W. Ward, N. P. Economou, R. Hill, R. Percival, L. Farkas, S. McVey, An Introduction to the Helium Ion Microscope, in: AIP Conference Proceedings, Vol. 931, 2007, pp. 489–496. doi:10.1063/1.2799423.

[19] R. Hill, F. H. M. Faridur Rahman, Advances in helium ion microscopy, Nuclear Instruments and Methods in Physics Research Section A: Accelerators, Spectrometers, Detectors and Associated Equipment 645 (1) (2011) 96–101. doi:10.1016/j.nima.2010.12.123.

[20] G. Hlawacek, V. Veligura, R. van Gastel, B. Poelsema, Helium ion microscopy, Journal of Vacuum Science & Technology B: Microelectronics and Nanometer Structures 32 (2) (2014) 020801. doi:10.1116/1.4863676.

[21] D. Emmrich, A. Beyer, A. Nadzeyka, S. Bauerdick, J. C. Meyer, J. Kotakoski, A. Gölzhäuser, Nanopore fabrication and characterization by helium ion microscopy, Applied Physics Letters 108 (16) (2016) 163103. doi:10.1063/1.4947277.

[22] T. Wirtz, N. Vanhove, L. Pillatsch, D. Dowsett, S. Sijbrandij, J. A. Notte, Towards secondary ion mass spectrometry on the helium ion microscope: An experimental and simulation based feasibility study with He^+ and Ne^+ bombardment, Applied Physics Letters 101 (4) (2012) 041601. doi:10.1063/1.4739240.

[23] L. Pillatsch, N. Vanhove, D. Dowsett, S. Sijbrandij, J. A. Notte, T. Wirtz, Study and optimisation of SIMS performed with He^+ and Ne^+ bombardment, Applied Surface Science 282 (2013) 908–913. doi:10.1016/j.apsusc.2013.06.088.

[24] D. Dowsett, T. Wirtz, N. Vanhove, L. Pillatsch, S. Sijbrandij, J. A. Notte, Secondary ion mass spectrometry on the helium ion microscope: A feasibility study of ion extraction, Journal of Vacuum Science & Technology B: Microelectronics and Nanometer Structures 30 (6) (2012) 06F602. doi:10.1116/1.4754309.

[25] P. Philipp, L. Rzeznik, T. Wirtz, Numerical investigation of depth profiling capabilities of helium and neon ions in ion microscopy, Beilstein Journal of Nanotechnology 7 (2016) 1749–1760. doi:10.3762/bjnano.7.168.

[26] N. Klingner, R. Heller, G. Hlawacek, J. von Borany, J. Notte, J. Huang, S. Facsko, Nanometer scale elemental analysis in the helium ion microscope using time of flight spectrometry, Ultramicroscopy 162 (2016) 91–97. doi:10.1016/j.ultramic.2015.12.005.

[27] N. Klingner, R. Heller, G. Hlawacek, J. von Borany, S. Facsko, Nanometer Scale Time of Flight Back Scattering Spectrometry in the Helium Ion Microscope, Microscopy and Microanalysis 22 (Suppl 3) (2016) 618–619. doi:10.1017/S1431927616003949.

[28] R. Heller, N. Klingner, G. Hlawacek, Backscattering Spectrometry in the Helium Ion Microscope: Imaging Elemental Compositions on the nm Scale, in: G. Hlawacek, A. Gölzhäuser (Eds.), Helium Ion Microscopy, NanoScience and Technology, Springer International Publishing, Cham, 2016, Ch. 12, pp. 265–295. doi:10.1007/978-3-319-41990-9.

[29] T. Wirtz, D. Dowsett, J.-N. Audinot, S. Eswara, SIMS on the Helium Ion Microscope: a Powerful Tool for High-Resolution High-Sensitivity Nano-Analytics, Microscopy and Microanalysis 22 (Suppl 3) (2016) 160–161. doi:10.1017/S1431927616001653.

[30] T. Wirtz, D. Dowsett, P. Philipp, SIMS on the Helium Ion Microscope: A Powerful Tool for High-Resolution High-Sensitivity Nano-Analytics, in: G. Hlawacek, A. Gölzhäuser (Eds.), Helium Ion Microscopy, NanoScience and Technology, Springer International Publishing, Cham, 2016, Ch. 13. doi:10.1007/978-3-319-41990-9.

[31] D. Dowsett, T. Wirtz, Co-Registered In Situ Secondary Electron and Mass Spectral Imaging on the Helium Ion Microscope Demonstrated Using Lithium Titanate and Magnesium Oxide Nanoparticles, Analytical Chemistry 89 (17) (2017) 8957–8965. doi:10.1021/acs.analchem.7b01481.

[32] M. P. Seah, Resolution parameters for model functions used in surface analysis, Surface and Interface Analysis 33 (12) (2002) 950–953. doi:10.1002/sia.1452.

[33] M. L. Nietiadi, L. Sandoval, H. M. Urbassek, W. Möller, Sputtering of Si nanospheres, Physical Review B 90 (4) (2014) 045417. doi:10.1103/PhysRevB.90.045417.

[34] W. Möller, TRI3DYN Collisional computer simulation of the dynamic evolution of 3-dimensional nanostructures under ion irradiation, Nuclear Instruments and Methods in Physics Research Section B: Beam Interactions with Materials and Atoms 322 (2014) 23–33. doi:10.1016/j.nimb.2013.12.027.

[35] T. Wirtz, P. Philipp, J.-N. Audinot, D. Dowsett, S. Eswara, High-resolution high-sensitivity elemental imaging by secondary ion mass spectrometry: from traditional 2D and 3D imaging to correlative microscopy, Nanotechnology 26 (43) (2015) 434001. doi:10.1088/0957-4484/26/43/434001.

[36] T. Aoki, S. Chiba, J. Matsuo, I. Yamada, J. P. Biersack, Molecular dynamics and Monte-Carlo simulation of sputtering and mixing by ion irradiation, Nuclear Instruments and Methods in Physics Research, Section B: Beam Interactions with Materials and Atoms 180 (1-4) (2001) 312–316. doi:10.1016/S0168-583X(01)00437-2.

[37] P. Sigmund, Elements of Sputtering Theory, in: Nanofabrication by Ion-Beam Sputtering, no. September 2016, Pan Stanford Publishing, 2012, pp. 1–40. doi:10.1201/b13726-2.

[38] A. Johannes, H. Holland-Moritz, C. Ronning, Ion beam irradiation of nanostructures: sputtering, dopant incorporation, and dynamic annealing, Semiconductor Science and Technology 30 (3) (2015) 033001. doi:10.1088/0268-1242/30/3/033001.

[39] R. Livengood, S. Tan, Y. Greenzweig, J. Notte, S. McVey, Subsurface damage from helium ions as a function of dose, beam energy, and dose rate, Journal of Vacuum Science & Technology B, Nanotechnology and Microelectronics: Materials, Processing, Measurement, and Phenomena 27 (6) (2009) 3244. doi:10.1116/1.3237101.

[40] Y. Greenzweig, Y. Drezner, S. Tan, R. H. Livengood, A. Raveh, Current density profile characterization and analysis method for focused ion beam, Microelectronic Engineering 155 (2016) 19–24. doi:10.1016/j.mee.2016.01.016.

[41] Y. Drezner, Y. Greenzweig, S. Tan, R. H. Livengood, A. Raveh, High resolution TEM analysis of focused ion beam amorphized regions in single crystal siliconA complementary materials analysis of the teardrop method, Journal of Vacuum Science & Technology B, Nanotechnology and Microelectronics: Materials, Processing, Measurement, and Phenomena 35 (1) (2017) 011801.

doi:10.1116/1.4972050.
[42] E. Salançon, Z. Hammadi, R. Morin, A new approach to gas field ion sources, Ultramicroscopy 95 (2003) 183–188. doi:10.1016/S0304-3991(02)00315-7.
[43] W.-T. Chang, I.-S. Hwang, H.-S. Kuo, T.-Y. Fu, J.-L. Hou, C.-Y. Lin, T.-T. Tsong, Single-atom Tip as an Emitter of Gas Field Ion Source, Microscopy and Microanalysis 19 (S2) (2013) 382–383. doi:10.1017/S1431927613003905.
[44] M. E. Schmidt, A. Yasaka, M. Akabori, H. Mizuta, Nitrogen Gas Field Ion Source (GFIS) Focused Ion Beam (FIB) Secondary Electron Imaging: A First Look, Microscopy and Microanalysis 23 (04) (2017) 758–768. doi:10.1017/S1431927617000502.
[45] W.-c. Lai, C.-y. Lin, W.-T. Chang, P.-c. Li, T.-Y. Fu, C.-S. Chang, T. T. Tsong, I.-S. Hwang, Xenon gas field ion source from a single-atom tip, Nanotechnology 28 (25) (2017) 255301. doi:10.1088/1361-6528/aa6ed3.
[46] R. L. Hervig, F. K. Mazdab, P. Williams, Y. Guan, G. R. Huss, L. A. Leshin, Useful ion yields for Cameca IMS 3f and 6f SIMS: Limits on quantitative analysis, Chemical Geology 227 (1-2) (2006) 83–99. doi:10.1016/j.chemgeo.2005.09.008.
[47] K. S. S. Liu, C. W. Yong, B. J. Garrison, J. C. Vickerman, Molecular Dynamics Simulations of Particle Bombardment Induced Desorption Processes: Alkanethiolates on Au(111), The Journal of Physical Chemistry B 103 (16) (1999) 3195–3205. doi:10.1021/jp984071k.
[48] A. M. Spool, Interpretation of static secondary ion spectra, Surface and Interface Analysis 36 (3) (2004) 264–274. doi:10.1002/sia.1685.
[49] C. Xu, H. D. Lee, S. Shubeita, G. Liu, Y. Xu, L. Wielunski, J. Bloch, B. Yakshinskiy, E. Garfunkel, T. Gustafsson, L. C. Feldman, Atomic collisions in materials analysis, Oral presentation at the 26th International Conference on Atomic Collisions in Solids (ICACS), Debrecen, Hungary.
[50] M. H. Mendenhall, R. A. Weller, A time-of-flight spectrometer for medium energy ion scattering, Nuclear Instruments and Methods in Physics Research Section B: Beam Interactions with Materials and Atoms 40-41 (2) (1989) 1239–1243. doi:10.1016/0168-583X(89)90628-9.
[51] R. A. Weller, J. H. Arps, D. Pedersen, M. H. Mendenhall, A model of the intrinsic efficiency of a time-of-flight spectrometer for keV ions, Nuclear Instruments and Methods in Physics Research Section A: Accelerators, Spectrometers, Detectors and Associated Equipment 353 (1-3) (1994) 579–582.
[52] G. Betz, K. Wien, Energy and angular distributions of sputtered particles, International Journal of Mass Spectrometry and Ion Processes 140 (1) (1994) 1–110. doi:10.1016/0168-1176(94)04052-4.
[53] T. Kalvas, O. Tarvainen, T. Ropponen, O. Steczkiewicz, J. Ärje, H. Clark, IBSIMU: A three-dimensional simulation software for charged particle optics, Review of Scientific Instruments 81 (2) (2010) 02B703. doi:10.1063/1.3258608.
[54] M. L. Yu, Velocity Dependence of the Ionization Probability of Sputtered Atoms, Physical Review Letters 47 (18) (1981) 1325–1328. doi:10.1103/PhysRevLett.47.1325.
[55] N. D. Lang, Ionization probability of sputtered atoms, Physical Review B 27 (4) (1983) 2019–2029. doi:10.1103/PhysRevB.27.2019.
[56] J. K. Nørskov, B. I. Lundqvist, Secondary-ion emission probability in sputtering, Physical Review B 19 (11) (1979) 5661–5665. doi:10.1103/PhysRevB.19.5661.
[57] A. Wucher, Formation of atomic secondary ions in sputtering, Applied Surface Science 255 (4) (2008) 1194–1200. doi:10.1016/j.apsusc.2008.05.252.
[58] A. Wucher, B. Weidtmann, A. Duvenbeck, A microscopic view of secondary ion formation, Nuclear Instruments and Methods in Physics Research Section B: Beam Interactions with Materials and Atoms 303 (2013) 108–111. doi:10.1016/j.nimb.2012.12.020.
[59] K. Mahesh, On the temperature dependence of the Mössbauer effect, Nuclear Instruments and Methods 65 (3) (1968) 349–352. doi:10.1016/0029-554X(68)90119-5.
[60] K. Mahady, S. Tan, Y. Greenzweig, R. Livengood, A. Raveh, P. D. Rack, Monte Carlo simulations of nanoscale Ne(+) ion beam sputtering: investigating the influence of surface effects, interstitial formation, and the nanostructural evolution., Nanotechnology 28 (4) (2016) 045305. doi:10.1088/1361-6528/28/4/045305.
[61] R. Timilsina, S. Tan, R. Livengood, P. D. Rack, Monte Carlo simulations of nanoscale focused neon ion beam sputtering of copper: elucidating resolution limits and sub-surface damage, Nanotechnology 25 (48) (2014) 485704. doi:10.1088/0957-4484/25/48/485704.
[62] J. I. Goldstein, D. E. Newbury, P. Echlin, D. C. Joy, C. E. Lyman, E. Lifshin, L. Sawyer, J. R. Michael, Scanning Electron Microscopy and X-ray Microanalysis, Springer US, Boston, MA, 2003. doi:10.1007/978-1-4615-0215-9.
[63] D. C. Bell, Contrast Mechanisms and Image Formation in Helium Ion Microscopy, Microscopy and Microanalysis 15 (02) (2009) 147–153. doi:10.1017/S1431927609090138.
[64] T. Yamanaka, K. Inai, K. Ohya, T. Ishitani, Simulation of secondary electron emission in helium ion microscope for overcut and undercut line-edge patterns, in: J. A. Allgair, C. J. Raymond (Eds.), Nuclear Instruments and Methods in Physics Research, Section B: Beam Interactions with Materials and Atoms, Vol. 267, 2009, p. 72722L. doi:10.1117/12.813889.
[65] K. Ohya, T. Yamanaka, K. Inai, T. Ishitani, Comparison of secondary electron emission in helium ion microscope with gallium ion and electron microscopes, Nuclear Instruments and Methods in Physics Research Section B: Beam Interactions with Materials and Atoms 267 (4)

993 (2009) 584–589. doi:10.1016/j.nimb.2008.11.003.